

MANTIS

Citation for published version (APA):

Perek, A., Vijvers, W. A. J., Andrebe, Y., Classen, I. G. J., Duval, B. P., Galperti, C., Harrison, J. R., Linehan, B. L., Ravensbergen, T., Verhaegh, K., & de Baar, M. R. (2019). MANTIS: A real-time quantitative multispectral imaging system for fusion plasmas. *Review of Scientific Instruments*, 90(12), [123514].
<https://doi.org/10.1063/1.5115569>

DOI:

[10.1063/1.5115569](https://doi.org/10.1063/1.5115569)

Document status and date:

Published: 01/12/2019

Document Version:

Publisher's PDF, also known as Version of Record (includes final page, issue and volume numbers)

Please check the document version of this publication:

- A submitted manuscript is the version of the article upon submission and before peer-review. There can be important differences between the submitted version and the official published version of record. People interested in the research are advised to contact the author for the final version of the publication, or visit the DOI to the publisher's website.
- The final author version and the galley proof are versions of the publication after peer review.
- The final published version features the final layout of the paper including the volume, issue and page numbers.

[Link to publication](#)

General rights

Copyright and moral rights for the publications made accessible in the public portal are retained by the authors and/or other copyright owners and it is a condition of accessing publications that users recognise and abide by the legal requirements associated with these rights.

- Users may download and print one copy of any publication from the public portal for the purpose of private study or research.
- You may not further distribute the material or use it for any profit-making activity or commercial gain
- You may freely distribute the URL identifying the publication in the public portal.

If the publication is distributed under the terms of Article 25fa of the Dutch Copyright Act, indicated by the "Taverne" license above, please follow below link for the End User Agreement:

www.tue.nl/taverne

Take down policy

If you believe that this document breaches copyright please contact us at:





openaccess@tue.nl

providing details and we will investigate your claim.

MANTIS: A real-time quantitative multispectral imaging system for fusion plasmas

Cite as: Rev. Sci. Instrum. **90**, 123514 (2019); <https://doi.org/10.1063/1.5115569>

Submitted: 19 June 2019 . Accepted: 22 November 2019 . Published Online: 31 December 2019

A. Perek , W. A. J. Vijvers, Y. Andrebe, I. G. J. Classen, B. P. Duval, C. Galperti, J. R. Harrison , B. L. Linehan, T. Ravensbergen , K. Verhaegh , M. R. de Baar, TCV, and EUROfusion MST1 Teams



View Online



Export Citation



CrossMark

ARTICLES YOU MAY BE INTERESTED IN

[A radio-frequency spin-polarized scanning tunneling microscope](#)

Review of Scientific Instruments **90**, 123705 (2019); <https://doi.org/10.1063/1.5104317>

[A parametric method for correcting polluted plasma current signal and its application on Keda Torus eXperiment](#)

Review of Scientific Instruments **90**, 123513 (2019); <https://doi.org/10.1063/1.5121503>

[Development of continuous wave high voltage negative ion beam injector for tandem accelerator](#)

Review of Scientific Instruments **90**, 123314 (2019); <https://doi.org/10.1063/1.5128590>



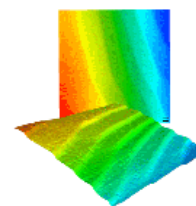
Nanopositioning
Systems



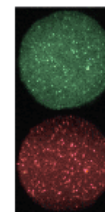
Modular
Motion Control



AFM and NSOM
Instruments



Single Molecule
Microscopes



MANTIS: A real-time quantitative multispectral imaging system for fusion plasmas

Cite as: *Rev. Sci. Instrum.* **90**, 123514 (2019); doi: [10.1063/1.5115569](https://doi.org/10.1063/1.5115569)

Submitted: 19 June 2019 • Accepted: 22 November 2019 •

Published Online: 31 December 2019



A. Perek,^{1,a)} W. A. J. Vijvers,¹ Y. Andrebe,² I. G. J. Classen,¹ B. P. Duval,² C. Galperti,² J. R. Harrison,³
B. L. Linehan,⁴ T. Ravensbergen,¹ K. Verhaegh,^{3,5} M. R. de Baar,¹ TCV,^{b)} and EUROfusion MST1 Teams^{c)}

AFFILIATIONS

¹Dutch Institute for Fundamental Energy Research (DIFFER), De Zaale 20, 5612 AJ Eindhoven, The Netherlands

²Ecole Polytechnique Fédérale de Lausanne (EPFL), Swiss Plasma Center (SPC), CH-1015 Lausanne, Switzerland

³CCFE, Culham Science Centre, Abingdon, Oxon OX14 3DB, United Kingdom

⁴Plasma Science and Fusion Center, Massachusetts Institute of Technology, 77 Massachusetts Avenue, NW17, Cambridge, Massachusetts 02139, USA

⁵York Plasma Institute, University of York, Heslington, York YO10 5DQ, United Kingdom

^{a)}a.perek@diffier.nl

^{b)}See the author list of S. Coda *et al.*, *Nucl. Fusion* **57**, 102011 (2017).

^{c)}See the author list of H. Meyer *et al.*, *Nucl. Fusion* **57**, 102014 (2017).

ABSTRACT

This work presents a novel, real-time capable, 10-channel Multispectral Advanced Narrowband Tokamak Imaging System installed on the TCV tokamak, MANTIS. Software and hardware requirements are presented together with the complete system architecture. The image quality of the system is assessed with emphasis on effects resulting from the narrowband interference filters. Some filters are found to create internal reflection images that are correlated with the filters' reflection coefficient. This was measured for selected filters where significant absorption (up to 65% within ~70 nm of the filter center) was measured. The majority of this was attributed to the filter's design, and several filters' performance is compared. Tailored real-time algorithms exploiting the system's capabilities are presented together with benchmarks comparing polling and event based synchronization. The real-time performance is demonstrated with a density ramp discharge performed on TCV. The behavior of spectral lines' emission from different plasma species and their interpretation are qualitatively described.

Published under license by AIP Publishing. <https://doi.org/10.1063/1.5115569>

I. INTRODUCTION

One of the long standing challenges in nuclear fusion research is the power exhaust. In future devices, a significant fraction of the fusion power will be diverted to a target surface in the form of heat and particle fluxes. In the case of the ITER tokamak, this will result in steady state heat loads to the target exceeding its material limit¹ of approximately 10 MW m^{-2} . To reduce the heat and particle fluxes, the divertor can be operated in the detached regime.² The line emission (of deuterium, intrinsic and extrinsic impurities) is increased and acts as a sink for the exhaust power emitting in the IR to the (X)UV region. A variety of atomic and molecular processes play an important role in reducing the heat and particle fluxes. The fundamentals of the processes involved in detachment and their

interaction are not yet well understood. At the TCV, detachment was previously studied with the use of line integrated spectroscopy,³ reciprocating probes,⁴ Langmuir probes,⁵ bolometry,⁶ IR cameras,^{7,8} and multispectral imaging.⁹

In this paper, we present a novel, 10-channel multispectral imaging (MSI) system with real-time capabilities, from now on referred to as Multispectral Advanced Narrowband Tokamak Imaging System (MANTIS). The aim of MANTIS is to obtain calibrated intensity images of different emission lines which will be used in collisional radiative modeling to obtain local plasma parameters such as density and temperature. Those parameters can then be used to study detachment in the divertor plasmas in various magnetic configurations with high spatial resolution and vessel coverage.

In addition to the physics analysis, the images will also serve as an input for model-based control algorithms for detachment control. The images will be used in real-time nontomographic inversions and real-time analysis to sense the locations of the detachment characteristic features such as emission fronts, ionization, and recycling regions. The information will then be used in a feedback control loop for the detachment actuators within the plasma control system. Previous efforts of the detachment control efforts employed sensors based on rt-thomson¹⁰ and rt-bolometry.¹¹

The system's optical design¹² is based on a 4-channel Multi-spectral Imaging System (MSI)⁹ previously installed on TCV. The design was extended to 10 channels with a completely new mechanical design, relay optic, and cameras. Figure 1 presents the MANTIS optical cavity design illustrating its principle of operation. A previous report analyzed the prospect of having an imaging cavity allowing for 10 camera views.¹³

In MANTIS, the light is relayed from an object to the cavity entrance where an image is formed. Then, the light continues to a relay lens behind which the first interference filter is placed. The filter transmits a spectrally narrow band to the first camera objective. The remaining light is reflected from the filter's surface and imaged onto the first concave mirror below the cavity entrance. Thus, a spectrally narrow band of light is extracted and the remaining light propagates to the next channel. This process is then repeated over the cavity until the last channel is reached and the remaining light is dumped onto black paper to reduce stray light. To avoid accumulation of chromatic aberrations, the image is rotated 180° in each channel by a concave mirror reflection, thus canceling the aberrations in every other channel.

In this paper, we address questions concerning the triggering, real-time algorithms, and their performance for multispectral imaging systems. We also address the design of the interference filters for the optical cavity imaging systems. The system's performance and

typical settings are presented on a density ramp discharge performed on TCV.

This paper is organized as follows: the hardware requirements and system's capabilities are described in Sec. II. Section III assesses the image quality of the system with emphasis on effects resulting from the narrowband interference filters. Two triggering schemes and their implementation are presented in Sec. IV. Utilizing those schemes, a real-time algorithm was developed (Sec. V with its performance benchmark in Sec. V A). In Sec. VI, the data acquired during a density ramp discharge is presented together with the performance of the real-time Auto Exposure Auto Gain (AEAG) feature.

II. HARDWARE AND TECHNICAL REQUIREMENTS

The aims of MANTIS can be divided into two areas: the passive acquisition of quantitative multispectral data for physics studies and a sensor for model based control in real-time. These two applications lead to two sets of requirements for the system that need to be simultaneously met. In this section, we analyze these sets of requirements, the optical design and system design, and compare with the system's capabilities.

The first set was formulated from spectroscopic observations with the use of the Divertor Spectroscopy System³ (DSS) installed on TCV. The DSS provides specially resolved spectroscopy for the divertor plasmas at a high dynamic range. The DSS data show that the brightness of the emission lines can vary by orders of magnitude throughout the discharge. This is true especially in the detachment studies where the density is increased through fueling^{3,14,15} or impurity seeding.¹⁶ To match those changes in brightness during the discharge, the system should be capable of altering the exposure time and gain in real-time. This also ensures an optimal signal to noise ratio throughout the discharge. Apart from the dynamic changes in brightness, the system should also be able to simultaneously observe both relatively dim and bright lines. An example of this is D_{α} , which can be 1000 times brighter than D_{ϵ} . In the case of MANTIS, each emission line falls on a different camera sensor. This should be exploited by acquiring data at different frame rates, exposures, and gains, depending on whether the acquisition is photon limited or camera frame rate limited. The time resolution should allow resolving between Edge Localized Modes (ELMs) and inter-ELM periods during ELMy H-mode operation. The system should have a spatial resolution of ≈ 5 mm to resolve features in the plasma such as hollow emission profiles, sharp emission gradients, and tile edges for camera calibration.

The second set of requirements originates from the control system aims. The system should be capable of real-time image processing. The delay between frame acquisition and its availability for processing should be negligible ($<1\%$) when compared to the acquisition cycle time. During the processing phase, the system should minimize the central processing unit (CPU) time spent on acquisition tasks. The system should be able to process the images in parallel. This should interface with the Digital Control System (SCD)¹⁷⁻¹⁹ which can actuate on the divertor plasmas, e.g., through the voltage on TCV's gas valves.

Both applications require stable data transfer for all cameras with a sufficient amount of computational time for both control and acquisition tasks. This should be achieved with a real-time Hardware

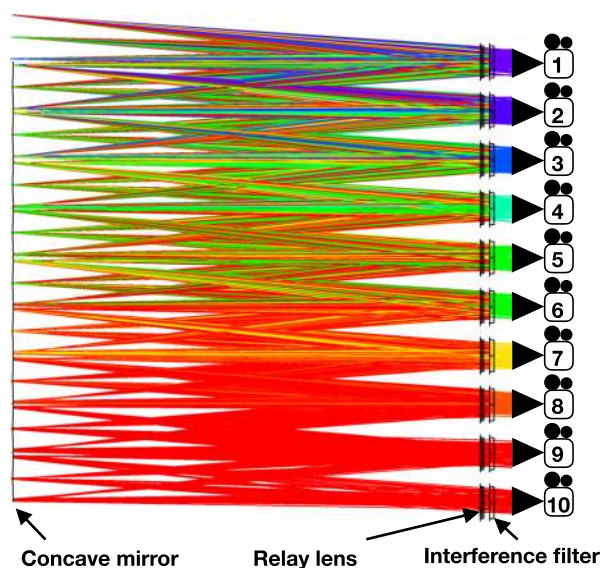


FIG. 1. Zemax ray tracing of MANTIS optical cavity design.

Interface Code (HIC) that should be easily configurable for different run scenarios in between the discharges.

A. Implementation

To meet the hardware requirements, the system was equipped with 10 xiX PCIe cameras with Sony IMX252 sensors. One advantage of such cost-effective CMOS camera sensors, crucial for our application, is that they can be read out and controlled (e.g., gain/exposure) in real-time. Considering the emission in the divertor and the magnification of 1:360, their size, dynamic range, and quantum efficiency are sufficient for obtaining 2D images of bright emission lines (D_{α} , C III, and n = 5, 6 and, 7 Balmer lines) at a sufficient temporal resolution (200 Hz–2000 Hz). Relevant specifications of the sensor can be found in Table I.

The cameras are connected to a switch provided together with the cameras by Ximea. The switch can connect up to 12 PCIe gen2x2 data streams which are aggregated into a single PCIe gen3x8 interface. Then, the data are sent through a 50 m long optical fiber to a host adapter in a PCIe bus of the ASUS Prime X299-Deluxe motherboard. The cameras use the PCIe interface to directly access the memory, allowing for data streaming directly to the RAM without the CPU involvement. The system was equipped with a 64 GB G.Skill Trident Z quad channel DDR4 memory. The motherboard hosts a 14-core Intel Core i9-7940-X with the intention of assigning one core per camera stream, one core for communication to the cameras, one core for the real-time linux kernel, and two cores for data aggregation, control algorithms, and communication with the SCD.

The hardware is managed with a Hardware Interface Code (HIC) which is aimed to be robust and configurable for different frame rates and number of cameras. The HIC manages setup and communication with the cameras, arms and disarms the trigger, delivers frames to the processing threads, migrates processed data between the threads, interacts with the TCV's digital control system,^{17–19} times its own performance, and saves the data to storage. The layout of the hardware and data migration paths for the real-time phase is presented in Fig. 2. Following the flow of a frame through the system, at first, the camera receives a hardware trigger and starts to expose the sensor. Once the exposure is finished, the frame is moved to a readout buffer, read out, and transferred via PCIe direct memory access (DMA) to a ring of buffers in the RAM. The use of the PCIe bus provides 6.4 Gbps uplink from each camera directly to the RAM of the acquisition PCs. Once the frame is delivered, the processing starts with a dynamically linked shared object library, Proc.so. The libraries are compiled versions of the image processing algorithms developed in Matlab Simulink. The

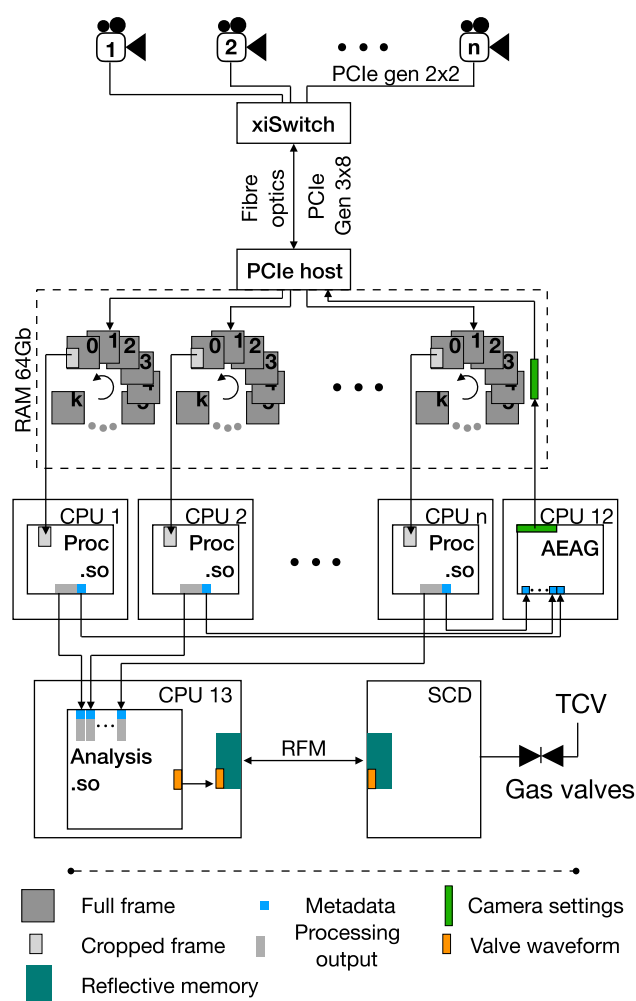


FIG. 2. Schematic overview of the real-time phase of the MANTIS. AEAG—Auto Exposure Auto Gain, RFM—Reflective Memory.

processing output is then transferred to the Analysis.so where the data are aggregated and the output for the SCD is prepared. Then, the output is passed to the SCD through a reflective memory card which allows for low latency (<1 ms) communication between nodes of the SCD. A detailed description of the hardware interface code can be found in Sec. V.

If the photon flux is sufficiently high, the limiting factor on the speed of acquisition is the camera sensor readout time. The sensor is read out in a line by line fashion. To increase the maximum acquisition frequency, the number of readout lines can be decreased by binning in the sensor's height by 2 and limiting the readout to a small Region Of Interest (ROI). This technical aspect is exploited in the MANTIS relay optic design by rotating the image by 90°. This way, the poloidal image of the plasma ends up horizontally on the landscape image of the sensor, while the binning now occurs in the radial direction. The readout also skips every other column on the sensor to reduce the amount of data for the real-time processing. Skipping

TABLE I. Relevant of the Sony IMX252 sensor.

Feature	Spec
Pixel resolution (px)	2064 × 1544, 1032 × 772
Pixel size (μm)	3.45 × 3.45
ADC (bit)	8, 10, 12
Dynamic range (dB)	70.9
Shutter type	Global

TABLE II. Frame rates calculated for selected frame widths using Eq. (1).

width (px)	8 bit (Hz)	10 bit (Hz)	12 bit (Hz)
376	800	700	450
276	1100	950	600
132	2000	1750	1100

is an optional step which can be substituted with postprocessing binning to improve the uniformity of the image.

Another factor playing an important role in the acquisition speed is the bit depth of the Analog to Digital Converter (ADC) used. The time required to digitize a single row of the sensor is called the line period; its effect on the maximum number of Frames Per Second (FPS) can be expressed as

$$FPS_{max} = \frac{1}{(w + 38)L_p}, \quad (1)$$

where w is the width in pixels of the readout ROI in the portrait orientation and L_p is the line period, i.e., readout time of a single line which is a function of the bit depth $L_p^{8bit} = 2.89 \mu s$, $L_p^{10bit} = 3.28 \mu s$, and $L_p^{12bit} = 5.29 \mu s$. Table II presents maximum frame rates for selected image widths.

With the current emissivities measured during TCV discharges, acquisition frequency of 1000 Hz can be used for monitoring the brightest emission lines on TCV such as D_{α} , C III, and N II. Acquisition frequency of 200 Hz can be used for monitoring $n = 5, 6,$ and 7 Balmer lines and most emissions of intrinsic helium. The frame rates for impurities are strongly dependent on vessel conditions and impurity seeding/puffing rates. With planned upgrades on interference filters as well as the TCV baffle upgrade, which is expected to lead to higher densities, the emissions as well as signals measured by MANTIS are expected to increase. This will lead to higher frame rates for currently photon-limited measurements. In the case of camera sensor limited frame rates, Fig. 3 presents TCV's lower divertor region imaged by MANTIS with vessel coverage corresponding to frame rates in Table II.

III. NARROWBAND FILTERS

One of the main advantages of the cavity over comparable beam splitter designs is the light retention. In the latter case, the light on every channel is split into two equal parts: one part for the camera and one part propagating to the next split. This results in a rapid decrease in the light intensity with an increase in the channel number. Contrary to the beam splitter systems, in MANTIS optical cavity, the incident light that is not passed by the filter should be reflected to the next channel. In this way, the light intensity losses are minimal.

Clear drawbacks of this design are accumulated absorbance and image degradation. In the MANTIS cavity, the light is reflected 18 times to reach the last camera. Half of those reflections take place on silver coated concave mirrors with the reflection coefficient $>98\%$ for the range $450\text{--}750$ nm and $>88\%$ for the range $380\text{--}450$ nm. Remaining reflections take place on the surfaces of the interference filters. In our previous analysis of the optical performance of the system,¹³ the interference filters were substituted with high quality flat mirrors.

In this section, the effects of the interference filters are investigated. To observe those effects on resolution and image sharpness, MANTIS was used to image an edge spatial frequency response test chart as a resolution target. Small ROIs of the target highlighting relevant observations are presented in Fig. 4(a). The first row presents channels 1–5, while the remaining channels are presented in the second row. The resolution targets do not show significant image degradation for the first two channels. Images from channels 3 and 4 present clear echo images. The echoes appear as the original image translated and superimposed. The number of the echoes decreases for channels 5–7, while channel 8 is echo free. Most of the echoes are also missing in channel 9 which collects light without a filter. Additional observations indicated that the echoes are created for specific filters, especially if the two filters are close (tens of nanometer) in the bandpass wavelength, thus hinting that the echo images are filter and wavelength dependent. The ordering of the filters was also found to play an important role in the echo image creation.

To study those dependencies, a number of filter configurations were explored. Figure 4(b) presents the result of replacing the 434.3 nm filter by a flat mirror. The images clearly show that the

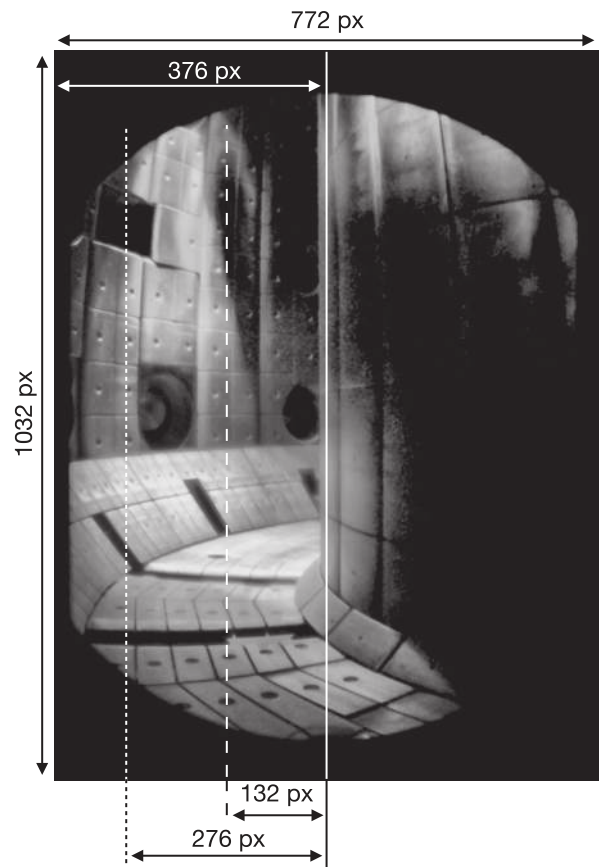


FIG. 3. High dynamic range image of the TCV's vacuum vessel imaged by MANTIS. The image consists of multiple images at different exposures; a 4×4 median filter was applied to reduce noise.

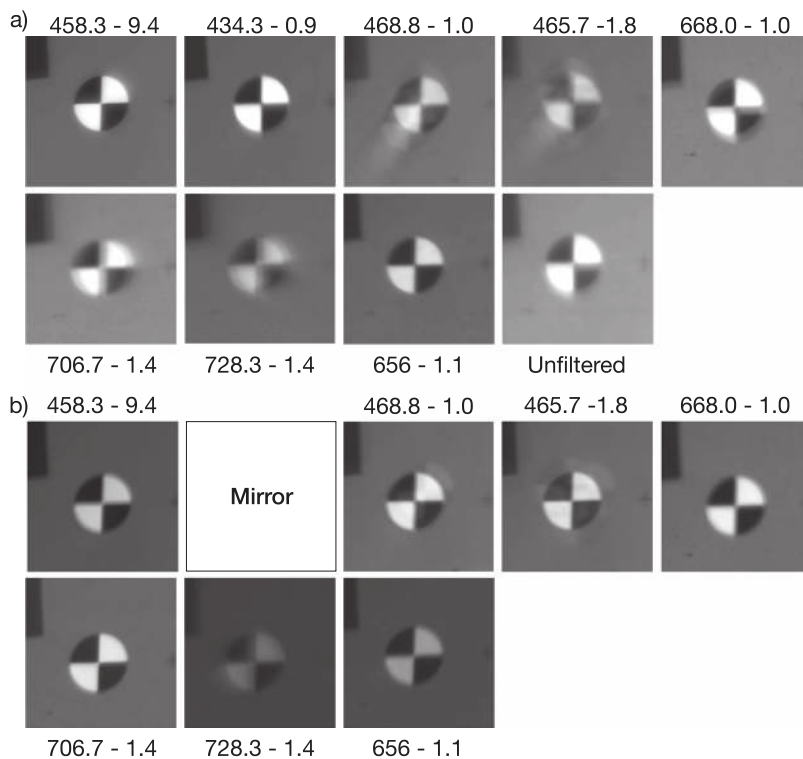


FIG. 4. Selected region of interest of a resolution chart for two proposed filter sets: (a) only interference filters were used; (b) the second filter of the set (a) was replaced with a mirror. The region of interest corresponds to the center of the divertor view. Full images of the chart are available online as supplementary data. The diameter of the registration mark was 40 mm. Filter specification format: central wavelength - bandwidth, both in nm, e.g., 458.3 - 9.4.

majority of the echoes originate from the replaced filter. This result shows that a single filter can introduce echo images to a number of other filters. It is worth mentioning that none of the filters have antireflective coating at the back side. The filters' surface roughness, transmitted/reflected waveform error and parallelism of the filter's surfaces that would normally render them unsuitable for imaging systems.

To further improve our understanding of the filters, the light retention in the cavity was measured. To do this measurement, each filter was replaced with flat mirrors starting with the first channel. During this test, the cameras were imaging an incandescent light source through an integrating sphere. When the first filter was replaced by a mirror, the sensor count in channels 3 and 4 increased to ~175% of the baseline configuration presented in Fig. 4(a). Replacement of the second filter further increased the signal levels for channels 3 and 4 to ~270% and ~250% of the baseline, respectively. At the same time, the filters in channels 5–8 showed only 10%–20% increase in the signal. When the filter in channel 6 was replaced, the light intensity in channel 7 increased from ~120% to ~170% of the baseline. This wavelength dependent absorption appears to be close to the filter's bandpass—this observation also appears to be true for the echo images.

The correlation between the echo images and localized absorption can be used as a proxy to derive an optimal filter configuration. To achieve that, the reflection coefficients of some of the filters were measured. The setup consisted of an integrating sphere with an incandescent light source. The light was reflected from the filter under 3° angle, mimicking the cavity design. Reflected light was

collected with custom collection optics to a fiber and passed to an OceanOptics spectrometer. As a reference for the measurement, a flat mirror (99.9% reflective) was used. The measurement error was estimated to be below 5%, based on the repeatability of the test.

The results of the reflection coefficient measurement are presented in Fig. 5. The reflection curves clearly show absorption near the filter's bandpass over ~70 nm in both directions. The filters at central wavelengths of 706.7 and 728.3 fall within each other's absorption region, which according to the proxy should result in mutual echo image creation. This prediction was observed during filter permutation studies using only 706.7 and 728.3; those filters were found to echo each other, regardless of the configuration. The ordering of the filters presented in Fig. 4 was selected as a permutation, minimizing the echo images. The same order of the filters can be derived from Fig. 5 as one of the absorption minimizing configurations.

The figure also shows that the 668 nm filter has desirable characteristics of blocking by reflection instead of absorption. The differences between those four filters were found in their design. The 668 nm filter was manufactured using only dielectric coating for light rejection, while the remaining 3 filters use both dielectric and metal coatings. The presence of two reflective coatings can explain the echo images, especially if the coatings are split between the two sides of the filter. As the light passes through the filter, it can be partially absorbed before it is reflected at the back side. If the reflection of that light occurs on both front and back surfaces, the absorption could indicate the wavelength range which is partially reflected on both surfaces simultaneously. This can explain the link between

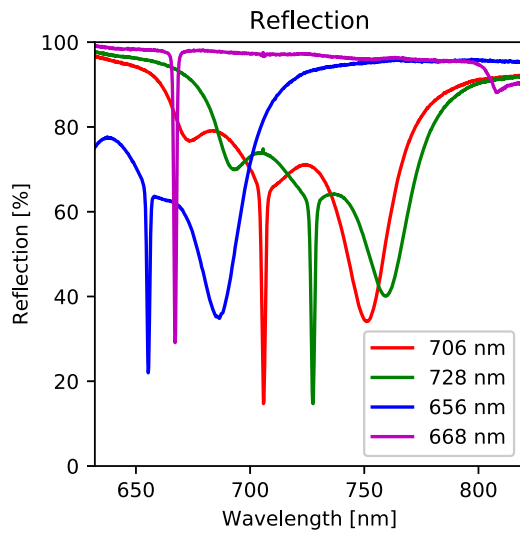


FIG. 5. Reflection coefficient of the filter surface measured at 3° angle of incidence with the use of an integrating sphere with an incandescent light source.

absorption and the echo images. To test this design characteristic, a new batch of filters was ordered for various wavelengths using only dielectric coating for blocking. Some of the new filters were found to have 10%–20% absorption around the bandpass, producing an echo image on other filters within that band. However, the echo images were not as pronounced as in the case of the filters presented in Fig. 4. Some of the filters were found to have a high reflection coefficient, following the characteristics of the 668 nm filter. The source of those differences in reflections/absorptions using the same filter design remains unexplained within this work. Further testing is planned to measure the transmission and reflection curves for all the used filters in the visible spectrum.

IV. TRIGGERING

The acquisition of an individual frame is triggered with a 5 V hardware trigger supplied through a single input in the xiSwitch to all of the cameras simultaneously. To facilitate the need for different frame rates at different cameras, the input trigger is multiplied by a burst of N frames on each camera individually. The burst of frames allows for synchronous start of acquisition between the cameras at trigger number k if

$$k \bmod \frac{N_1}{N_2} = 0. \quad (2)$$

N_1 and N_2 are the numbers of burst frames of two different cameras; the condition holds, provided that $N_1 \geq N_2$. This scheme allows for synchronization of the start of the exposure phase between all cameras on every common trigger. This does not mean that the time intervals at which the system acquires all cameras are identical. However, assuming that the emission is quasistatic during the exposure times, synchronicity is achieved. In case when the camera is not ready to start the next burst, the trigger is latched and the next burst is acquired as soon as possible. The beginning of each individual exposure is time stamped by the camera's Field Programmable

TABLE III. Different modes of trigger operation.

Mode	Clock drift	Auto gain	Auto exposure
Multiple frame rates	$<45 \mu\text{s/s}$	YES	NO
Single frame rate	$<1 \mu\text{s/s}$	YES	YES

Gate Array (FPGA) allowing for individual timing measurements with $1 \mu\text{s}$ resolution.

The triggering solution was implemented using Red Pitaya which is used as a programmable FPGA-based function generator. The Red Pitaya is programmed over the Ethernet via the Standard Commands for Programmable Instruments (SCPI) to output a pulse train of 5 V pulses triggered by an external TTL pulse delivered by the TCV's infrastructure. Due to limitations on the Red Pitaya's output and input voltages, a custom breakout board was built to interface between the TCV, Red Pitaya, and cameras.

The triggering solution was tested using timestamps of individual cameras to measure the synchronization of the start of the exposure phase. The test was performed at the trigger rate of 100 Hz with bursts of 1, 2, and 4 frames, resulting in 100, 200, and 400 Hz parallel acquisitions. The measurement showed that the start of the exposures on cameras at the same frame rate remains synchronous within $5 \mu\text{s}$ without drifts. In the case of a comparison between different frame rates, the cameras are found to drift apart with $<45 \mu\text{s/s}$. The drift between the cameras results in a known shift at the start of the exposure.

An alternative operational mode is to run all cameras with the same number of burst frames, $N = 1$. This mode provides $<5 \mu\text{s}$ accuracy for all cameras. Additionally, it allows for a change in the exposure time in real-time without affecting the synchronization of the start of the exposure. This mode ensures that the dynamic range of the sensor can be fully optimized throughout the discharge, maximizing signal to noise ratios.

The advantages of the two modes of operation could be combined in the future, provided that the hardware modifications will be performed. Table III presents the main features of different modes of trigger operation.

V. REAL-TIME ALGORITHM

One of the main requirements of the HIC is to provide maximum flexibility to support all possible camera and real-time processing setups within a reasonable parameter space. The algorithm is divided into n parallel processing threads for n cameras, assigning one thread per CPU core per camera, one thread to manage the Auto Exposure Auto Gain (AEAG) feature, and two analysis/control threads that combine outputs of the processing threads. The layout of the connections in the HIC is presented in Fig. 2. The HIC is divided into two stages of execution. The first stage processes the images to reduce the amount of data and obtain information on the location of the divertor leg together with the emission intensity. The second stage can take the outputs of the first stage, combine, and feed them to the control algorithms running locally. The output of the second stage can then be transmitted to the SCD which can actuate on the plasma. The output could also be used to constrain the real-time magnetic equilibrium reconstruction running within the SCD.

The first stage processing threads start their cycle by polling on the last pixel of the DMA buffer of the next available frame. Once the last pixel is nonzero, the processing starts on each thread individually synchronized to its own camera buffer. Currently, the real-time processing involves the AEAG algorithm which crops and copies a region of interest to the prepared buffer. To remove high frequency noise such as salt and pepper noise, the copy is processed with a 3 pixel radius median blur convolution filter. The value and the location of the maximum count are found and saved to an output buffer. Next, the second stage threads are informed that the output buffer is available. The cycle ends, and the processing thread is free to return to DMA buffer polling for the next frame.

The second stage of the HIC currently consists of two threads, the Analysis and the AEAG. The AEAG thread constantly checks the status of all processing threads in search of any available outputs. Once an output is found, it averages the maximum count from last 5 frames of that thread to evaluate the signal level. The averaging results in a time blur that serves as ELM and transient event rejection. An alternative option would be to use the median instead of the average. Then, a decision is made how the exposure and/or gain should be changed based on the AEAG algorithm. Currently, the decision is based on the ratio of the current count rate and desirable count rate obtained through the following relation:

$$cts \propto exposure \cdot 10^{gain[db]/20}. \quad (3)$$

At first, the exposure is changed to match the desired count level. If the exposure reaches its maximum limit, the gain is increased. If the new camera parameters differ sufficiently from the current values, the changes are communicated and the thread proceeds to adjust the next camera.

The second example of the second stage is the Analysis thread. Contrary to the AEAG thread, it must wait until all required data are available. This is performed by waiting only for the output on the camera threads meeting the synchronization condition presented in Eq. 2. The Analysis thread can be treated as a camera thread which must be synchronous to all other threads on all frames. Thus, it must run at the speed of the fastest camera. This also implies that the data from slower cameras will be used in multiple iterations. The schematic of the time behavior of the HIC is presented in Fig. 6.

In the case of the multiple frame rate scenario presented in Sec. IV, the time available for processing can range from 2500 μ s to 10 000 μ s, corresponding to 400 Hz and 100 Hz acquisitions, respectively. Provided that identical processing is performed on all processing threads, the system can be left with a significant amount of idle time on the 100 Hz threads. To exploit the remaining resources, the algorithm divides available processing time into timeslots corresponding to the fastest frame rate. This approach allows for allocation of additional tasks starting in any available timeslots.

A. Timing

The time performance of a real-time system can be measured in two categories: the time elapsed performing computations and the ability to repeat the “lap time” of a single iteration consistently. The measurements are also used to track the behavior of the real-time algorithm. To accurately measure the passage of time, the Time Stamp Counter (TSC) was used. It is a 64 bit register counting the

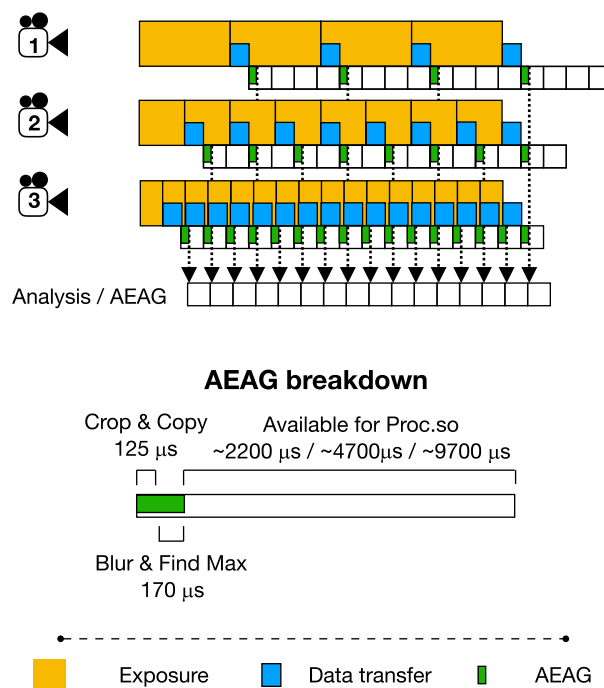


FIG. 6. Schematic of the real-time algorithm timing at 100, 200, and 400 Hz acquisition. Auto Exposure Auto Gain (AEAG) breakdown for 580 \times 428 px region of interest.

number of clock ticks on a nominal CPU frequency since reset. Provided that the TSC is constant and shared between the CPU cores, it can be used to measure the passage of time between two measurement points. Then, the TSC difference is subtracted, and the nominal CPU frequency is used to convert the clock ticks to elapsed time.

To perform timing tests, a synthetic repeat option was created. This repeat performs the entire discharge cycle including arming cameras, loading parameters, and processing libraries. As an additional step, it downloads the data from the storage server. Then, it places it in additional buffer rings identical to those set up by the cameras. During the real-time phase, as the cameras acquire images of stray light inside MANTIS, the processing threads swap the incoming images for the data recorded during the experiments. In this way, the system can “replay” an entire acquisition and processing with a completely negligible overhead. This feature proves to be extremely useful for development and testing.

In this section, the timing tests evaluate the system’s ability to consistently repeat a single iteration of acquisition and processing. The starting point of the iteration is the frame delivery to the DMA buffer. This point is also the source of synchronization between all of the camera threads. Thus, its performance is crucial to the whole system. In this test, we compare two different synchronization methods between the processing and the DMA buffers, namely, polling and events.

To measure the consistency of the real-time code execution, the cameras were triggered in the single trigger mode. This mode ensures $<1 \mu$ s synchronization between cameras introducing

minimum uncertainty. The test was set up as a synthetic repeat of the shot TCV No. 62135 during which the system acquired data for 2.25 s at 200 Hz on 9 cameras simultaneously.

To test event based synchronization, the cameras communicated with the HIC via PCIe events handled by the interrupt controller on the motherboard. This approach uses minimum resources during idle time. However, it does not provide high determinism on when the frame arrives. Additionally, this approach scales unfavorably with an increasing number of running cameras and their frame rate.

To test polling based synchronization, the addresses of the DMA buffers were obtained for each camera by its processing thread. Then, each processing thread polls on the last pixel of its DMA frame buffer of the next frame to determine whether the frame is ready to be processed. This approach has an additional benefit of occupying 100% of the processor core, forcing it to stay on task at all times.

Figure 7 presents time difference between the delivery time of frames n and $n + 1$ for polling and event based synchronization. The comparison shows that polling can deliver $<1 \mu\text{s}$ synchronization, while events resulted in $<1000 \mu\text{s}$ synchronization. This result shows that polling is indeed a much more deterministic option for synchronization of the cameras. The uncertainty is found to be comparable to the triggering mode uncertainty, which is the lowest achievable, given the test setup.

Additional tests revealed that in the event based synchronization, the information about frame arrival became increasingly delayed and uncertain with the increasing number of events. This might be caused by the events issued by multiple cameras to a single controller. An additional experiment with polling showed that a single microsecond of idle time introduced in between the polls increased the uncertainty from $<1 \mu\text{s}$ to $<150 \mu\text{s}$. This result could be explained by the CPU switching tasks in the idle time. Given that our application requires negligible delays ($<1\%$ of the frame time) between acquisition and availability, polling based synchronization was selected for the HIC. All of the following measurements use polling.

The next step is to measure the repeatability of the processing time. If the start of the processing is accurately determined by polling, the end time of the image processing carries the information about introduced jitter. This can be observed in Fig. 7(c), presenting the frame-to-frame time interval for processing the output. The figure shows that the output varies within $\lesssim 25 \mu\text{s}$ which is the jitter introduced by processing.

To measure the jitter introduced by the interthread communication, the same frame-to-frame measurements were performed at the analysis threads. The results can be found in Fig. 7, showing that negligible jitter is introduced as the data arrive in the Analysis thread.

Those results show that MANTIS cameras can be used for real-time applications, provided that the polling scheme is used in acquisition. If each camera can be assigned a dedicated CPU core, this approach is also unaffected by the number of cameras and the frame rate.

During the TCV experiments, the AEAG algorithm is enabled by default at $t = 200 \text{ ms}$ to adapt the gain and the exposure time. At first, the algorithm overshoots both settings to the maximum, resulting in a temporary saturation on some of the cameras as the

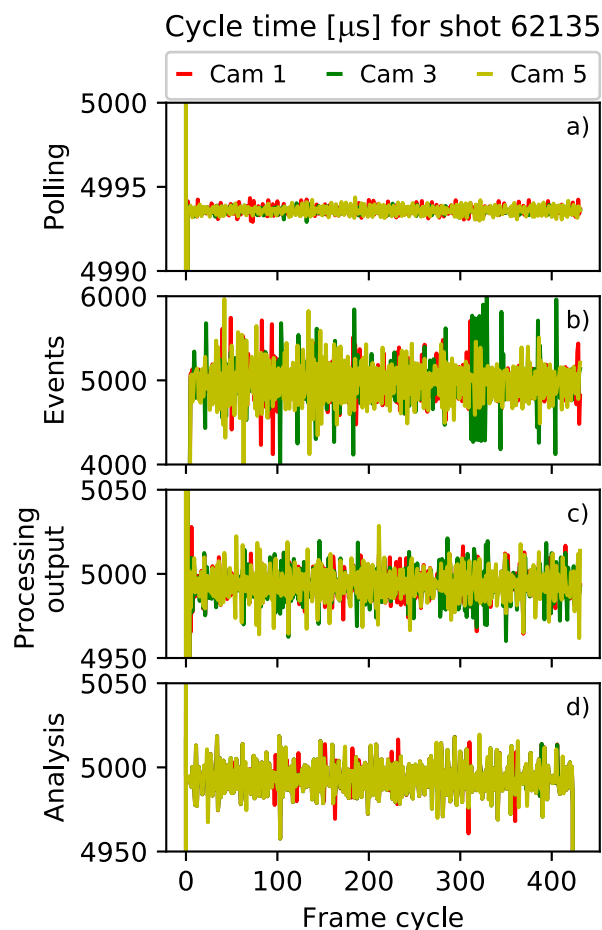


FIG. 7. Measurement of the time elapsed in the frame to frame cycle: (a) The time difference between retrieving two consecutive frames using polling on the last pixel. (b) The time difference between retrieving two consecutive frames using PCIe events. (c) The time difference in obtaining two consecutive processing outputs with the frame obtained by polling. (d) The time difference in delivering two consecutive processing outputs to the Analysis thread with the frame obtained by polling.

plasma brightness was increasing. After the initial overshoot, the algorithm managed to keep the maximum count in the frame around the desired 3300 counts throughout the discharge. The algorithm changed the camera settings only if the maximum count fell below or exceeded the deviation of 500 counts from the desired signal level. This can be observed in the oscillatory motion of the maximum count in subplot 8(a). The information about the gain and exposure was used to calculate the maximum count per second at 0 dB gain using Eq. (3). The maximum count per second presented in Fig. 8(d) shows that the changes to the exposure and gain resulted in smooth relative intensity traces. This was expected, given that the sensor characterization of the Photon Transfer Curves (PTCs) did not reveal any significant nonlinearity with the gain. Gain stability was tested by altering the gain between 0, 12 and, 24 dB on each consecutive frame during 200 Hz acquisition for 2 s. This test also did not find any significant deviation from the expected signals.

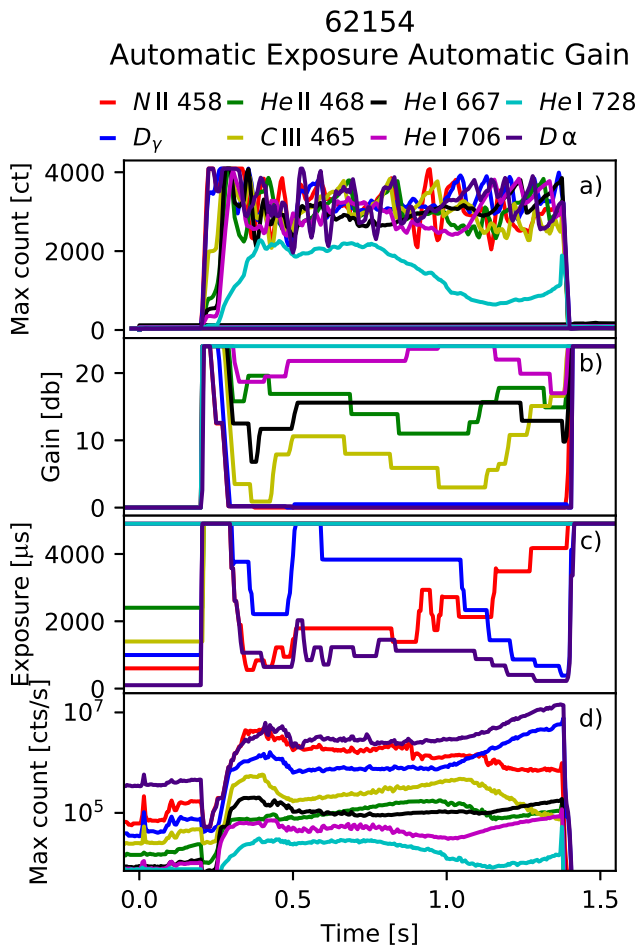


FIG. 8. Behavior of the Auto Exposure Auto Gain algorithm on shot 62154. (a) The maximum count rate found by the algorithm within the region of interest. (b) Gain set on each camera individually as a function of time. (c) Exposure time set on each individual camera as a function of time. (d) The maximum count from (a) normalized through the gain and the exposure to gain = 0 dB.

Thus, the MANTIS can also be used to obtain 2D distributions of the absolute intensity of light passed through the filters. The system was absolutely calibrated using an incandescent source with an integrating sphere as a reference.

VI. DETACHMENT EXPERIMENT

The MANTIS is installed on the TCV tokamak, since shot 61600. The system is located at a lower tangential port, viewing the plasma in the clockwise direction. The field of view of the system is presented in Fig. 3. The system is routinely operated at 200 FPS, allowing for the synchronous AEAG feature; higher frame rates are operated with the Auto Gain feature alone. The filter set contains 8 narrow band filters with FWHM in the range 1–4 nm. The central wavelengths and filter widths are presented in Fig. 4(a).

This section presents multispectral imaging observations in shot 62154 which has an ohmic density ramp at a plasma current

of $I_p = 320$ kA, outer strike point at major radius of $R_t = 0.90$ m, and flux expansion of $f_x = 5$. This discharge was a part of the MST1 campaign studying alternative divertor configurations in the L-mode.

Figure 9 presents the time evolution of the selected ROIs for D_γ and C III emission images. The top row presents the D_γ emission along the divertor leg. At first, the emission connects the X-point with the tokamak floor where it emits a wider, toroidally symmetric band. As the time advances and in this case the density increases, the emission front lifts from the floor resulting in a “split” of emission between the floor and the divertor leg. This “split” in the Balmer line emission is caused by a separation of the excitation emission (moving toward the X-point as the ionization peak moves) and recombination emission appearing near the target as the divertor temperatures are driven to a couple of electron volt.^{3,20} The recombination emission is expected to increase with the divertor densities which are expected after the TCV baffle upgrade.^{21–23} In the images from $t = 905$ ms, emission from the private flux region becomes more pronounced connecting the tokamak floor with the central column below the inner strike point. At the same time, the toroidal ring of D_γ emission at the tokamak floor widens.

Another interesting feature can be observed in D_γ at $t = 1005$ ms; the divertor leg appears to be bifurcated in the radially outward direction. This can also be observed in the floor emission in the toroidally symmetric rings. This feature was observed in multiple discharges on TCV in hydrogen and helium emission lines with MANTIS. The bottom row of Fig. 9 presents C III triplet at 465 nm. Contrary to D_γ , the emission occurs mainly along the divertor leg and the plasma boundary, which is expected as C III emission usually originates at the hottest temperature regions (e.g., near the separatrix) where C^{2+} ions still appear.

As the time advances and the density in the core increases, the emission front of the C III line clearly lifts from the target and moves toward the X-point. The C III light is also free of bifurcation observed in D_γ . Thus, it clearly shows the location of the peak of the emission region. The peak in the emission of the C III region, or some fall-off length below this (e.g., emission front), is correlated with the radiation front measured by bolometry^{14,15} as most of the radiative losses during nonseeded experiments on TCV are due to carbon impurities. Therefore, controlling the C III emission region in carbon devices without extrinsic seeding could be useful for controlling the radiative region. The location of the emission region can be found after analysis with the use of tomographic inversions using the camera calibration with Calcam.²⁴ Unfortunately, the tomographic inversions are computationally intensive and cannot be run in real-time on MANTIS PC. The plasma boundary reconstruction and emission front tracking can also be performed with nontomographic image processing methods in real-time. The first results together with a possible algorithm can be found in Ref. 25.

Figure 10 presents a compilation of 9 channels of the MANTIS for the shot 62154 with the filters, as described in Fig. 4. The compilation presents different behaviors of different plasma species. N II, C III, and He II appear to have clear emission fronts. D_γ presents radiation mostly at the floor of the tokamak, while D_α emission clearly occurs in the divertor leg. Helium images present different heights of the emission fronts for neutral and ionized helium. This could be an indication that in the lower part of the divertor, the

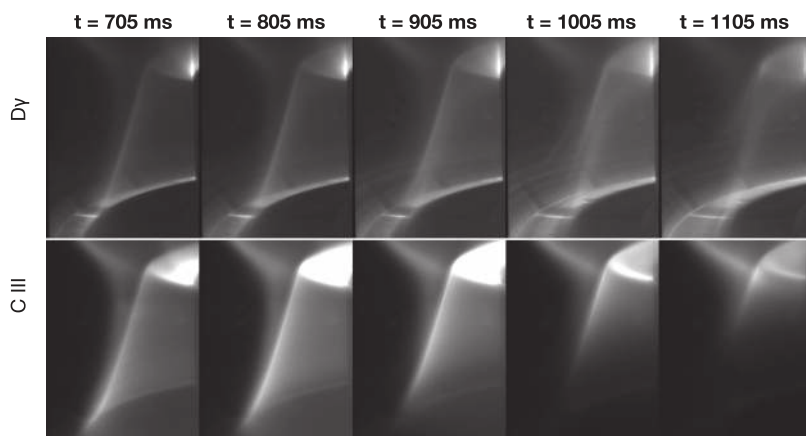


FIG. 9. Shot 62154, the selected region of interest of raw images from C III and D_γ filtered cameras.

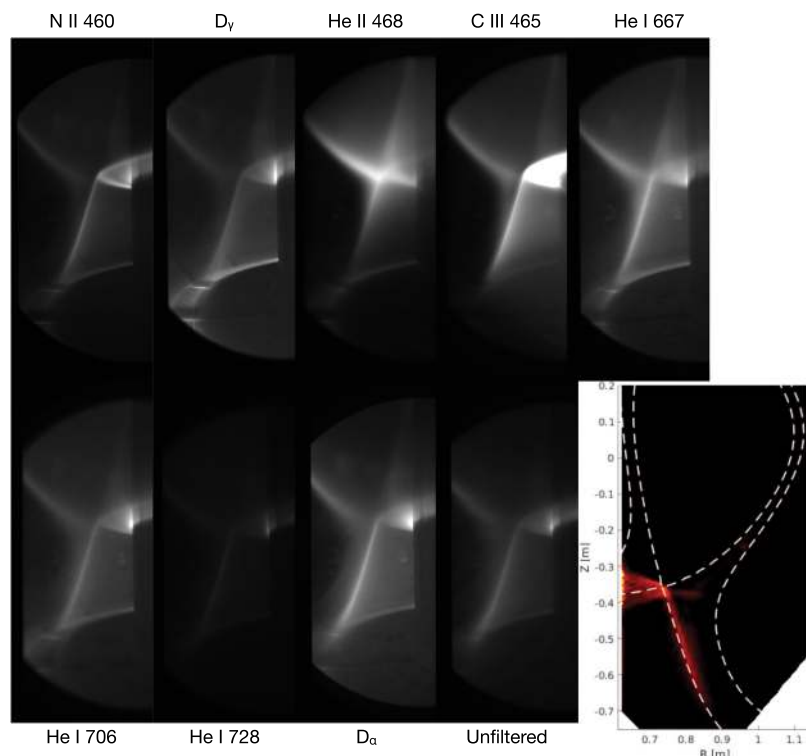


FIG. 10. Compiled image of shot 62154, $t = 900$ ms with 8 filters installed and channel 9 collecting all of the remaining light. The magnetic equilibrium (dashed lines) is presented together with the tomographic inversion of the C III image using Calcam.

temperature is too low for He^{1+} and is thus dominated by neutral helium. However, significant He I emission still occurs upward of the He II emission front. This depends on charged and metastable particle transport of helium.

VII. CONCLUSIONS

The MANTIS was presented together with its technical requirements and capabilities. The image quality was assessed for 9 channels, emphasizing creation of the echo images. The problem was investigated, and the majority of echo images were linked to a

single filter which was found to have significant absorption close to its transmission band. The reflection coefficient of selected filters was measured. Significant localized dips in reflection were found around the transmission bands of the filters. A correlation between filter configurations minimizing both absorption and echo images was also found. The filter design review found that the combination of metallic and dielectric coating was correlated with the wavelength dependent absorption. The split of the reflection occurring partially on both surfaces with absorption in between can explain the link between the echo image creation and the wavelength dependent absorption.

The real-time capabilities of the system were presented. An algorithm capable of running different cameras at different frame rates was implemented and tested. The tests compared two different approaches to the real-time frame acquisition and processing, namely, polling and events. The polling approach was found to be 3 orders of magnitude more stable than the events providing negligible uncertainty in the frame acquisition. Real-time image processing was demonstrated and timed on multiple cameras simultaneously. The processing time was used for implementation of an AEAG feature optimizing the dynamic range of the sensor throughout the discharge. The processing time was found to be stable during the experiment; the minimum overhead of 125 μ s was found for the real-time processing assuming a relatively large ROI.

A single discharge was presented showing the movement of the C III emission front together with D_{γ} emission. The performance of the AEAG feature demonstrated the system's capability to change exposure and gain in real-time. The record of the changes allowed us to reconstruct the relative intensity traces of the maximum value. The relative intensity can be converted to the absolute intensity which can be used together with the tomographic inversions to obtain absolutely calibrated 2D emissivity maps. Those emissivity maps can be used to constrain collisional radiative modeling and obtain 2D maps of plasma parameters during the divertor detachment. The parameters can then be used for both control purposes and physics studies.

SUPPLEMENTARY MATERIAL

See the [supplementary material](#) for complete images of the resolution targets presented in [Fig. 4](#).

ACKNOWLEDGMENTS

The first author would like to thank the TCV team and especially Mirko Wensing for their invaluable input and help in MANTIS installation and commissioning. This work has been carried out within the framework of the EUROfusion Consortium and has received funding from the Euratom research and training program 2014-2018 and 2019-2020 under Grant Agreement No. 633053. The views and opinions expressed herein do not necessarily reflect those of the European Commission. This work was supported in part by the Swiss National Science Foundation.

REFERENCES

- 1 A. Loarte, B. Lipschultz, A. S. Kukushkin, G. F. Matthews, P. C. Stangeby, N. Asakura, G. F. Counsell, G. Federici, A. Kallenbach, K. Krieger, A. Mahdavi, V. Philipps, D. Reiter, J. Roth, J. Strachan, D. Whyte, R. Doerner, T. Eich, W. Fundamenski, A. Herrmann, M. Fenstermacher, P. Ghendrih, M. Groth, A. Kirschner, S. Konoshima, B. Labombard, P. Lang, A. W. Leonard, P. Monier-Garbet, R. Neu, H. Pacher, B. Pegourie, R. A. Pitts, S. Takamura, J. Terry, and E. Tsrone, "Chapter 4: Power and particle control," *Nucl. Fusion* **47**(6), S203 (2007).
- 2 S. I. Krashennikov, A. S. Kukushkin, and A. A. Pshenov, "Divertor plasma detachment," *Phys. Plasmas* **23**(5), 055602 (2016).
- 3 K. Verhaegh, B. Lipschultz, B. P. Duval, J. R. Harrison, H. Reimerdes, C. Theiler, B. Labit, R. Maurizio, C. Marini, F. Nespoli, U. Sheikh, C. K. Tsui, N. Vianello, and W. A. J. Vijvers, "Spectroscopic investigations of divertor detachment in TCV," *Nucl. Mater. Energy* **12**, 1112-1117 (2017).
- 4 C. K. Tsui, J. A. Boedo, J. R. Myra, B. Duval, B. Labit, C. Theiler, N. Vianello, W. A. J. Vijvers, H. Reimerdes, S. Coda, O. Février, J. R. Harrison, J. Horacek,

- B. Lipschultz, R. Maurizio, F. Nespoli, U. Sheikh, K. Verhaegh, and N. Walkden, "Filamentary velocity scaling validation in the TCV tokamak," *Phys. Plasmas* **25**(7), 072506 (2018).
- 5 O. Février, C. Theiler, H. De Oliveira, B. Labit, N. Fedorczak, and A. Bailod, "Analysis of wall-embedded Langmuir probe signals in different conditions on the tokamak à configuration variable," *Rev. Sci. Instrum.* **89**(5), 053502 (2018).
- 6 H. Weisen, R. Behn, Y. Camenen, S. Coda, A. Degeling, B. P. Duval, E. Fable, I. Furno, B. Joye, X. Llobet, Y. Martin, A. Pochelon, Y. Peysson, R. A. Pitts, A. Sushkov, A. Zabolotsky, and S. Zoletnik, "Multi-chord diagnostics on the TCV tokamak," in *The 2nd German-Polish Conference on Plasma Diagnostics for Fusion and Applications (GPPD-2004)*, Cracow, Poland, 2014, pp. 1-6.
- 7 F. Nespoli, "Scrape-off layer physics in limited plasmas in TCV," Ph.D. thesis, EPFL, Lausanne, 2017.
- 8 R. Maurizio, B. P. Duval, J. Harrison, B. Labit, B. Lipschultz, H. Reimerdes, C. Theiler, K. Verhaegh, and W. Vijvers, "Divertor heat flux characterisation during detachment experiments in TCV," in *44th EPS Conference on Plasma Physics* (2017), p. 215001.
- 9 B. L. Linehan, R. T. Mumgaard, M. Wensing, K. Verhaegh, Y. Andrebe, J. R. Harrison, B. P. Duval, and C. Theiler, "The multi-spectral imaging diagnostic," *Rev. Sci. Instrum.* **89**, 103503 (2018).
- 10 D. Eldon, E. Kolemen, J. L. Barton, A. R. Briesemeister, D. A. Humphreys, A. W. Leonard, R. Maingi, M. A. Makowski, A. G. McLean, A. L. Moser, and P. C. Stangeby, "Controlling marginally detached divertor plasmas," *Nucl. Fusion* **57**(6), 066039 (2017).
- 11 D. Eldon, E. Kolemen, D. A. Humphreys, A. W. Hyatt, A. E. Järvinen, A. W. Leonard, A. G. McLean, A. L. Moser, T. W. Petrie, and M. L. Walke, "Advances in radiated power control at DIII-D," *Nucl. Mater. Energy* **18**, 285-290 (2019).
- 12 R. T. Mumgaard, "Engineering upgrades to the motional stark effect diagnostic on Alcator C-Mod engineering," Ph.D. thesis, Massachusetts Institute of Technology, 2015.
- 13 W. A. J. Vijvers, R. T. Mumgaard, Y. Andrebe, I. G. J. Classen, and B. P. Duval, "Conceptual design and proof-of-principle testing of the real-time multispectral imaging system MANTIS," *J. Instrum.* **12**, C12058 (2017).
- 14 C. Theiler, B. Lipschultz, J. Harrison, B. Labit, H. Reimerdes, C. Tsui, W. A. J. Vijvers, J. A. Boedo, B. P. Duval, S. Elmore, P. Innocente, U. Kruezi, T. Lunt, R. Maurizio, F. Nespoli, U. Sheikh, A. J. Thornton, S. H. M. van Limpt, K. Verhaegh, and N. Vianello, "Results from recent detachment experiments in alternative divertor configurations on TCV," *Nucl. Fusion* **57**(7), 072008 (2017).
- 15 J. R. Harrison, W. A. J. Vijvers, C. Theiler, B. P. Duval, S. Elmore, B. Labit, B. Lipschultz, S. H. M. van Limpt, S. W. Lisgo, C. K. Tsui, H. Reimerdes, U. Sheikh, K. H. A. Verhaegh, M. Wischmeier, and U. Sheikh, "Detachment evolution on the TCV tokamak," *Nucl. Mater. Energy* **12**, 1071-1076 (2016).
- 16 J. R. Harrison, C. Theiler, O. Février, H. de Oliveira, R. Maurizio, K. Verhaegh, A. Perek, A. Karpushov, B. Lipschultz, B. P. Duval, J. R. Harrison, W. A. J. Vijvers, C. Theiler, B. P. Duval, X. Feng, S. S. Henderson, B. Labit, B. L. Linehan, A. Merle, H. Reimerdes, U. Sheikh, C. K. Tsui, W. A. J. Vijvers, C. Wuethrich, TCV Team, and EUROfusion MST1 Team, "Progress toward divertor detachment in TCV H-mode discharges," *Plasma Phys. Controlled Fusion* **61**, 065024 (2019).
- 17 F. Felici, H. B. Le, J. I. Paley, B. P. Duval, S. Coda, J. Moret, A. Bortolon, L. Federspiel, T. P. Goodman, G. Hommen, A. Karpushov, F. Piras, A. Pitzschke, J. Romero, G. Sevillano, O. Sauter, W. Vijvers, and TCV Team, "Development of real-time plasma analysis and control algorithms for the TCV tokamak using SIMULINK," *Fusion Eng. Des.* **89**, 165-176 (2014).
- 18 F. Felici, T. P. Goodman, C. Galperti, H. Anand, B. P. Duval, S. Coda, J.-M. Moret, O. Sauter, T. Blanken, D. Kim, and E. Maljaars, "Distributed digital real-time control system for the TCV tokamak and its applications," *Nucl. Fusion* **57**(5), 056005 (2017).
- 19 C. Galperti, S. Coda, B. P. Duval, X. Llobet, P. Milne, O. Sauter, J. M. Moret, and D. Testa, "Integration of a real-time node for magnetic perturbations signal analysis in the distributed digital control system of the TCV tokamak," *IEEE Trans. Nucl. Sci.* **64**(6), 1446-1454 (2017).
- 20 K. Verhaegh, B. Lipschultz, B. Duval, O. Février, A. Fil, C. Theiler, M. Wensing, C. Bowman, D. S. Gahle, J. Harrison, L. Benoit, C. Marini, R. Maurizio,

H. de Oliveira, H. Reimerdes, U. Sheikh, C. Tsui, N. Vianello, and W. Vijvers, "An improved understanding of the roles of atomic processes and power balance in divertor target ion current loss during detachment," *Nucl. Fusion* **59**, 126038 (2018).

²¹A. Fasoli *et al.*, "TCV heating and divertor upgrades," *Nucl. Fusion* **60**, 016019 (2019).

²²H. Reimerdes, S. Alberti, P. Blanchard, P. Bruzzone, R. Chavan, S. Coda, B. P. Duval, A. Fasoli, B. Labit, B. Lipschultz, T. Lunt, Y. Martin, J.-M. Moret, U. Sheikh, B. Sudki, D. Testa, C. Theiler, M. Toussaint, D. Uglietti, N. Vianello, and M. Wischmeier, "TCV divertor upgrade for alternative magnetic configurations," *Nucl. Mater. Energy* **12**, 1106–1111 (2017).

²³M. Wensing, B. P. Duval, O. Février, A. Fil, D. Galassi, E. Havlickova, A. Perek, H. Reimerdes, C. Theiler, K. Verhaegh, and M. Wischmeier, "SOLPS-ITER simulations of the TCV divertor upgrade," *Plasma Phys. Controlled Fusion* **61**, 085029 (2019).

²⁴S. Silburn, J. Harrison, M. Smithies, A. Wynn, T. Farley, and J. Cavalier (2018). "Calcam," Zenodo. <http://doi.org/10.5281/zenodo.1478555>

²⁵T. Ravensbergen, M. van Berkel, S. A. Silburn, J. R. Harrison, A. Perek, K. Verhaegh, W. A. J. Vijvers, C. Theiler, A. Kirk, M. R. de Baar, EUROfusion MST1 Team, and TCV Team, "Real-time detection of the radiation front during divertor detachment using multi-spectral imaging," *Nucl. Fusion* (submitted).